

## Continuous Gravitational Waves from Supersoft X-ray Sources: Promising Targets for deci-Hz Detectors

MAYUSREE DAS<sup>\*, 1, \*</sup>, TOMASZ BULIK<sup>†, 2, †</sup>, SREETA ROY<sup>§, 2</sup> AND BANIBRATA MUKHOPADHYAY<sup>‡, 3, 1, ‡</sup><sup>1</sup>Joint Astronomy Programme, Department of Physics, Indian Institute of Science, Bangalore, 560012, India<sup>2</sup>Astronomical Observatory, University of Warsaw, Al. Ujazdowskie 4, 00478 Warsaw, Poland<sup>3</sup>Department of Physics, Indian Institute of Science, Bangalore, 560012, India

(Received XXX; Revised YYY; Accepted ZZZ)

## ABSTRACT

Supersoft X-ray sources (SSSs) host white dwarfs (WDs) accreting at rates that sustain steady nuclear burning, driving rapid mass growth, radial contraction, and magnetic field amplification. Angular-momentum transfer from the accretion disk naturally spins up the WD, while the amplified internal magnetic field induces a non-axisymmetric deformation in presence of a misaligned rotation. Such WDs emits continuous gravitational waves (CGWs). We model the coupled evolutions of stellar mass, spin, and magnetic structure in accreting WDs in SSSs with MESA, and compute the resulting quadrupolar deformation with the Einstein-Maxwell solver XNS. We show that WDs in SSSs, particularly near the end of thermal timescale mass transfer and close to the Chandrasekhar mass limit, produce CGWs predominantly in the deci-Hz band accessible to planned detectors such as DECIGO, BBO, Deci-Hz, ALIA, and LGWA, and are distinguishable from other Galactic CGW sources such as AM CVn systems, detached double WDs, and isolated WDs. Well-studied SSSs such as CAL 83 and RX J0019+2156 can be detectable, enabling targeted CGW measurements that directly probe WD's internal magnetic fields and rotation, while blind searches can reveal hundreds of obscured SSSs otherwise missed in soft X-rays and map the hidden population of accreting, rapidly rotating, magnetized WDs in nearby galaxies. A CGW detection from WDs in SSSs could also identify potential pre-explosion Type Ia progenitors.

## 1. INTRODUCTION

Supersoft X-ray sources (SSSs) were first identified by ROSAT with luminosity  $\sim 10^{37}\text{--}10^{38}$  erg s $^{-1}$  and effective temperature of 10 $^5$  K ( $kT \sim 20\text{--}50$  eV; Trümper et al. 1991; Greiner 1991). Their optical counterparts confirm that they are close binaries with orbital periods of  $\sim 8$  hr–1.4 d. Later they were understood as interacting binaries where a white dwarf (WD) accretes H-rich material at  $\dot{M}_{\text{WD}} \sim (1\text{--}5) \times 10^{-7} M_{\odot} \text{ yr}^{-1}$  from a slightly evolved main sequence star (MS), subgiant, or red-giant donor, sustaining stable H burning (van den Heuvel et al. 1992; Kahabka 1995; Nomoto et al. 2007; Wolf et al. 2013). A high mass transfer rate from the donor ( $\dot{M}_2$ ) arises during thermally unstable Roche-lobe overflow. When  $\dot{M}_2$  exceeds the WD's critical burning rate (set by the Eddington luminosity),  $\sim 60\text{--}80\%$  of the transferred mass is expelled in an optically thick wind, so that only  $\sim 20\text{--}40\%$  is retained by the WD, defining the actual accretion rate  $\dot{M}_{\text{WD}}$  (Hachisu & Kato 2003).

The supersoft X-ray luminosity is generated by energy released from steady nuclear burning on the WD surface rather than by the gravitational potential energy liberated by accretion, although absorption by circumstellar material associated with wind losses can modify the observed emission. At lower  $\dot{M}_2$ , nuclear burning becomes unstable, leading to recurrent novae with negligible mass retention, while at higher  $\dot{M}_2$  the burning envelope expands toward a red-giant like configuration that again drives strong winds (Nomoto 1979).

SSSs naturally emerge from  $\sim 5\text{--}8 M_{\odot}$  MS (primary) and  $\sim 1\text{--}3 M_{\odot}$  MS (secondary;  $M_2$ ) binary evolution (Rappaport et al. 1994; Hachisu et al. 1999). After an initial common-envelope episode, the primary becomes a CO/ONe WD in a compact orbit with secondary MS. After  $\sim 8/(M_2/M_{\odot})^2$  Gyr, the secondary evolves to fill its Roche lobe, and transfers mass on a thermal timescale onto the WD, producing the SSS phase (see Figure 1). If the WD is initially massive, stable accretion can grow it toward the Chandrasekhar limit, making SSSs plausible progenitors of  $\sim 10\text{--}30\%$  of Type Ia Supernovae (Rappaport et al. 1994; Hachisu et al. 1999). Otherwise, after thermal-timescale ( $\sim 3 \times 10^7 (M_2/M_{\odot})^{-2.3}$  yr),  $M_2$  drops below the steady-burning regime, after which the system transitions into late-SSS states such as V Sge-like sys-

<sup>\*</sup> mayusreedas@iisc.ac.in<sup>†</sup> tb@astrouw.edu.pl<sup>‡</sup> bm@iisc.ac.in

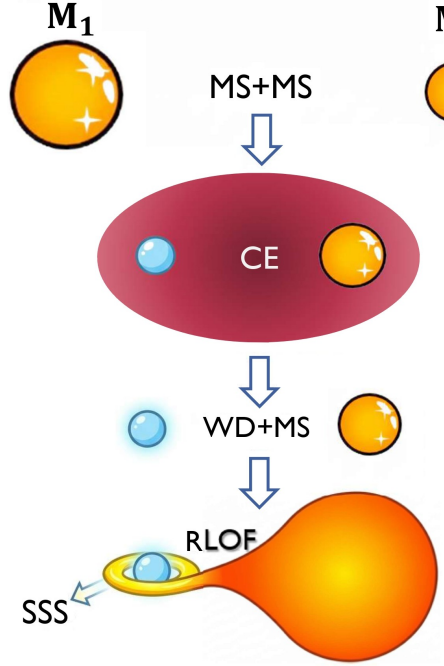


**Figure 1.** Cartoon illustration of the standard evolutionary channel leading to a SSS.

tems with accretion–wind cycle, symbiotic SSSs, or recurrent novae (e.g., U Sco) or eventually evolves into a double WD.

Population synthesis models predict existence of  $\gtrsim 1000$  SSSs in the Milky Way (MW) (Rappaport et al. 1994), but due to strong interstellar absorption in the Galactic plane only  $\sim 10$  are observed (van den Heuvel et al. 1992). In the Large Magellanic Cloud (LMC), in which direction interstellar column densities are lower,  $\sim 30$  SSSs are detected out of several hundreds (Rappaport et al. 1994). CAL 83 is the best studied prototypical SSS, alongside nearby Galactic systems such as RX J0019+2156 and RX J0925-4758 (Greiner 2000), however, the latter shows dense winds and transient jets consistent with intermittent accretion and wind regulated burning (Motch et al. 1994).

Steady accretion in SSSs increases the WD mass and leads to contraction of the stellar radius, amplifying the magnetic field through flux freezing, while angular momentum exchange with the accretion disk spins up the star (Ghosh & Lamb 1979b). In SSSs, steady accretion requires that the magnetic field remains below the propeller threshold (Ghosh 1995), so that the ram pressure of the inflowing matter exceeds the magnetic pressure and accretion onto the WD surface can proceed. Magnetic field amplification and spin-up therefore occur within this sub-propeller regime during the SSS phase, prior to any possible transition to propeller-dominated states at later evolutionary stages.

In such magnetized, spinning WDs residing in SSSs, anisotropic magnetic pressure induces a quadrupolar defor-

mation, and a misalignment between the magnetic and spin axes (obliquity angle  $\chi$ ) produces continuous gravitational waves (CGWs) at the spin frequency  $\nu$  and its harmonic  $2\nu$  (Bonazzola & Gourgoulhon 1996; Heyl 2000). Observed magnetic dichroism in several WDs (Putney 1992; Suto et al. 2023) confirms that oblique magnetic geometries ( $\chi \neq 0$ ) are common. Thus SSSs are favorable gravitational wave (GW) targets: continuous high accretion naturally couples WD mass growth, magnetic field amplification, and rotational spin-up – three key ingredients for persistent CGW emission. The CGW can be enhanced and thus highly plausible for detection near the end of the thermal timescale mass transfer phase or when the WD approaches the Chandrasekhar limit. Such signals may fall in the sensitivity windows and frequency range of planned/proposed GW missions including LISA (Colpi et al. 2024), DECIGO (Kawamura et al. 2021), the proposed Indian Deci-Hz detector (Rajesh K. Nayak et al., private communication)<sup>1</sup>, ALIA (Crowder & Cornish 2005), BBO (Cutler & Harms 2006), TianQin (Mei et al. 2021), LILA (Creighton et al. 2025), and LGWA (Ajith et al. 2024). Apart from CGW from the WD, SSSs also emit GW due to binary orbital evolution, which lies below the frequency range considered here; such orbital GW emission from accreting double WD binaries has been studied by Yi et al. (2024).

Detection of SSSs such as CAL 83 or RX J0019+2156 in CGWs could probe the WD’s internal magnetic field and angular velocity. Moreover, blind searches could reveal large hidden population of SSSs in the MW and LMC that remain invisible in soft X-rays otherwise due to interstellar absorption. Finally, if near-Chandrasekhar SSSs—plausible Type Ia progenitors, such as CAL 83 (hosting a  $\sim 1.3 M_{\odot}$  WD) are detected as CGW sources, they would provide a direct identification of a pre-explosion Type Ia progenitor. Type Ia supernova yet has not been observed to erupt from a system previously confirmed as a progenitor, so a pre-explosion CGW identification would offer a predictive path toward an eventual optical supernova discovery.

In this work, we link the evolution of accreting, magnetized, rapidly rotating WDs in SSSs to their CGW emission and assess detectability for both known systems and blind searches, extending our isolated WD study (Das et al. 2025); hereafter DMB2025). Section 2 outlines our stellar evolution models for the accreting WDs. Section 3 presents the magnetic deformation and CGW signal computed with the stellar structure solver and discusses their detectability with future detectors. We conclude by summarizing the implications of CGW detection for both known SSSs and the hidden SSS population.

<sup>1</sup> Based on representative noise PSD of a possible Indian deciHz mission, tentatively referred to as IndIGO-D.

## 2. MODELING AND EVOLUTION OF MAGNETIZED, ROTATING, ACCRETING WHITE DWARFS

### 2.1. Stellar Structure and Evolution with MESA

To model stellar evolution of magnetized, rotating, and accreting WDs, we employ MESA (Paxton et al. 2011). Thereafter, we first outline the stellar-structure and evolution equations involved in the standard (non-magnetic, non-rotating, non-accreting) configuration. These baseline equations form the reference framework to which rotation, magnetic fields, and accretion physics will be added in the following subsections. The stellar-structure equations in Lagrangian form (Paxton et al. 2011) are:

$$\frac{dr}{dm} = \frac{1}{4\pi r^2 \rho}, \quad (1)$$

$$\frac{dP}{dm} = -\frac{Gm}{4\pi r^4}, \quad (2)$$

$$\frac{dT}{dm} = -\frac{Gm}{4\pi r^4} \frac{T}{P} \nabla, \quad (3)$$

$$\frac{dL}{dm} = \epsilon_{\text{nucl}} - \epsilon_{\nu, \text{therm}} + \epsilon_{\text{grav}}, \quad (4)$$

$$\frac{dX}{dt} = \left( \frac{dX}{dt} \right)_{\text{burn}} + \frac{d}{dm} \left( \sigma \frac{dX}{dm} \right). \quad (5)$$

Here  $\nabla \equiv d \ln T / d \ln P$  is the temperature gradient,  $\epsilon_{\text{nucl}}$  is the nuclear energy generation rate per unit mass,  $\epsilon_{\nu, \text{therm}}$  is the neutrino energy loss rate per unit mass from thermal processes, and  $\epsilon_{\text{grav}}$  is the gravothermal energy generation rate per unit mass during compression or expansion (see Paxton et al. 2011),  $(dX/dt)_{\text{burn}}$  represents rate of changes in composition from nuclear burning,  $\sigma$  is the Lagrangian diffusion coefficient for compositional transport,  $\rho$  is the density,  $r$  is the radial coordinate and  $T$ ,  $P$ ,  $L$ , and  $X$  denote the temperature, pressure, luminosity, and compositional mass fraction, respectively. MESA solves the above equations in an adaptive, time-dependent Lagrangian framework with mass  $m$  as the independent coordinate, using the Skye equation of state (Jermyn et al. 2021) for the degenerate electron gas, with smooth transitions across partial and full degeneracy.

A key limitation of our present model is that we suppress steady H burning by setting  $\epsilon_{\text{nucl}} = 0$  and  $(dX/dt)_{\text{burn}} = 0$  for numerical stability, even though real SSS systems do undergo stable H burning producing He (the net effect is incorporated in Section 2.4). This may slightly alter envelope's temperature stratification but does not significantly affect the WD's radius, spin, or magnetic field, which we study here.

### 2.2. Magnetic Field

Having outlined the non-magnetic baseline structure, we now incorporate magnetic fields into the WD model. Because MESA does not solve Maxwell equations, the magnetic configuration must be supplied externally. We adopt the field

profiles obtained from the Einstein–Maxwell solver XNS (Soddueschi et al. 2021), modified for WDs in DMB2025 (this solver will be described in detail in Section 3). Observational and theoretical studies indicate that WDs may host strong internal toroidal components that dominate over the internal poloidal field (Wickramasinghe et al. 2014). Motivated by these stable configuration, we represent the internal toroidal field using the XNS-motivated prescription

$$B(r) = \mathcal{K} \rho r, \quad (6)$$

where  $\mathcal{K}$  sets the normalization. This scaling is similar to flux freezing, i.e.  $B \propto \rho r \propto M/r^{-2}$ , and thus  $B(r)$  enhances locally under contraction.

However, the magnetic field also decays through Ohmic and Hall dissipation (Heyl & Kulkarni 1998; Bhattacharya et al. 2022), i.e.,

$$\frac{dB(r)}{dt} = -B(r) \left( \frac{1}{t_{\text{ohm}}} + \frac{1}{t_{\text{Hall}}} \right), \quad (7)$$

with characteristic timescales (Goldreich & Reisenegger 1992; Cumming 2002)

$$t_{\text{ohm}} = (2.2 \times 10^{11} \text{ yr}) \rho_{c,9}^{1/3} R_8^{1/2} (\rho_{\text{avg}}/\rho_c), \quad (8)$$

$$t_{\text{Hall}} = (1.7 \times 10^{11} \text{ yr}) l_8^2 B_{m,12}^{-1} \rho_{c,9}, \quad (9)$$

where for any quantity  $X_n \equiv X/10^n$  in CGS units,  $B_m$  is the maximum magnetic field of a profile,  $R$  is WD's radius,  $\rho_{\text{avg}}$  and  $\rho_c$  are the average and central densities, respectively.

At each MESA timestep, we compute the magnetic profile  $B(r)$  using Equation (6) for the current stellar structure including contribution from magnetic pressure (see below). The field is then evolved over the timestep using Equation (7), and the normalization  $\mathcal{K}$  is updated accordingly, ensuring that the magnetic profile remains consistent with the changing WD structure while incorporating Ohmic and Hall dissipations.

An illustration of the magnetic field evolution for a WD of mass  $1.3 M_{\odot}$  that accretes and leads to  $1.4 M_{\odot}$  over  $\sim 10^6$  yr (details of accretion is in Section 2.4) is shown in Figure 2. As the star contracts during mass growth, an initial maximum internal field  $B_m \sim 10^{12}$  G, interpreted as a fossil field inherited from a strongly magnetized progenitor Ap/Bp stars (Ferrario et al. 2015; Quentin & Tout 2018; Mukhopadhyay & Bhattacharya 2022), is amplified further to  $\sim 10^{13}$  G. The corresponding magnetic to gravitational energy ratio increases from  $7 \times 10^{-7}$  to  $4 \times 10^{-4}$ . Over the shorter accretion timescale considered here, Ohmic and Hall diffusions are negligible, since their decay times in the degenerate interior are  $\gtrsim 10^8$ – $10^9$  yr, so the evolution is governed predominantly by compression rather than dissipation.

The internal field modeled here is toroidally dominated, with the surface strength being around four orders of magnitude weaker than  $B_m$  (see Figure 2). In addition, a one to two

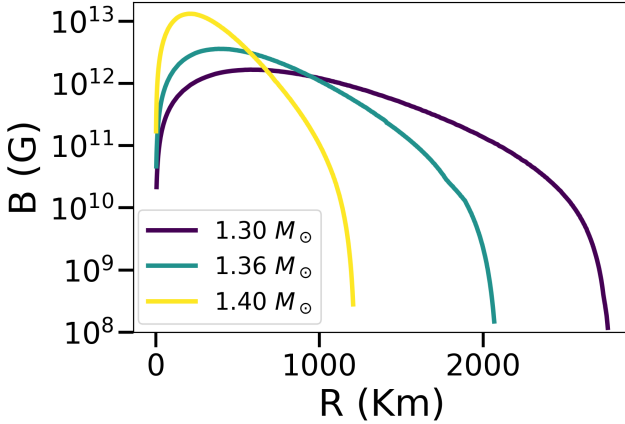


**Figure 2.** Radial profiles of the internal toroidal magnetic field  $B(r)$  at several stages along the accreting WD sequence (Section 2.4), showing the amplification of  $B$  due to mainly stellar contraction.

order(s) of magnitude weaker large-scale poloidal field is expected to be present: its polar amplitude  $B_p \approx B_m/10^{5-6}$  (Braithwaite & Spruit 2006; Braithwaite 2009). This exterior poloidal component is treated purely as an assumed dipole for radiation and disk-field coupling (to be discussed in Section 2.5); it is not included in the internal equilibrium computed by XNS or MESA (as effect is negligible to impact on stellar structure).

This evolving (internal) field also feeds back on the stellar structure through its pressure support. The internal toroidal magnetic field contributes to an additional pressure term and thus the total pressure in Equation (2) as

$$P = P_{\text{matter}} + \frac{B^2}{8\pi}, \quad (10)$$

where  $P_{\text{matter}}$  is the thermodynamic matter pressure. The magnetic pressure contribution  $B^2/8\pi$  is included in MESA through an `extra_pressure` term implemented in `other_pressure` routine of `run_star_extras` (Paxton et al. 2019), ensuring that the stellar structure remains consistent with the evolving magnetic field at each timestep.

### 2.3. Rotation

Having incorporated magnetic fields into the WD structure, we now include rotation, which modifies the stellar stratification. In MESA, rotation is treated using the shellular formalism of Endal & Sofia (1976), where each isobar is replaced by an equivalent sphere of radius  $r_p = (3V_p/4\pi)^{1/3}$ , with  $V_p$  the volume enclosed by the isobar. The continuity and energy conservation equations retain their usual form, while the hydrostatic equilibrium and energy transport equations acquire rotational correction factors  $f_P$  and  $f_T$ , respectively, that account for the reduction of effective gravity and the geometric distortion of equipotential surfaces (Paxton et al. 2013). The

modified Equations (2) and (3) are therefore

$$\frac{dP_p}{dm_p} = -\frac{Gm_p}{4\pi r_p^4} f_p, \quad \frac{dT_p}{dm_p} = -\frac{Gm_p}{4\pi r_p^4} \frac{T_p}{P_p} \nabla f_T. \quad (11)$$

Here  $m_p$ ,  $r_p$ ,  $P_p$ , and  $T_p$  are quantities averaged over an isobar.  $f_p$  and  $f_T$  depend on the surface-averaged effective gravity  $g_{\text{eff}} = g - \Omega^2 r_{\perp}$ , where  $r_{\perp}$  is the cylindrical (equatorial) distance from the rotation axis,  $\Omega$  is stars angular rotation rate. MESA (Paxton et al. 2013) adopts the analytical functions  $f_p(\Omega)$ ,  $f_T(\Omega)$  derived by Endal & Sofia (1976) in a one-dimensional (1D) form. In our models,  $\Omega$  remains well below the critical (break-up) limit, with  $\Omega/\Omega_{\text{crit}} \lesssim 0.01$ , so centrifugal distortion is minimal and  $f_p \simeq f_T \simeq 1$ , leaving the stellar structure close to non-rotating ones. Consistently, the ratio of rotational to gravitational energies remains small ( $\lesssim 0.1$ ), confirming that none of the models approach rotational instability.

### 2.4. Accretion

Having incorporated both magnetic fields and rotation into the WD structure, we now include mass accretion, as occurs in SSSs. In our models, the companion is not explicitly evolved; instead, the net accretion rate onto the WD,  $\dot{M}_{\text{WD}}$ , obtained after retention from the donor's mass transfer rate  $\dot{M}_2$ , is prescribed following Paxton et al. (2015). WD's mass  $M$  therefore increases as

$$M = M_{\star} + \dot{M}_{\text{WD}} dt, \quad (12)$$

where  $M_{\star}$  is the initial mass. Newly accreted material is added to the outermost mesh cell, after which MESA readjusts the model to re-establish hydrostatic and thermal equilibrium. Consistent with SSS conditions, we treat the accreted material as pure He. Although the transferred gas is H-rich, stable H burning at the characteristic SSS accretion rates ( $\dot{M}_{\text{WD}} \sim 10^{-7} M_{\odot} \text{ yr}^{-1}$ ) rapidly converts H to He (Nomoto et al. 2007; Wolf et al. 2013), on timescales much shorter than any structural timescale of the WD. As a result, the surface composition becomes effectively He-dominated, thus, treating the accreted material as pure He is a good approximation.

Matter transferred through Roche-lobe circularizes via angular-momentum conservation and forms a Keplerian accretion disk. Accretion proceeds as long as the inflowing matter can penetrate the stellar magnetosphere set by external dipolar field. The field then truncates the disk at a radius  $R_m$ , where magnetic pressure balances the inflow ram pressure; inside  $R_m$  the disk is disrupted and accretion proceeds along magnetic funnels, as described in the classical Ghosh-Lamb (GL) model (Ghosh & Lamb 1979a,b). This is shown as illustration in Figure 3. Although originally derived for neutron stars, this model is also applicable for WDs (Norton et al. 2004).  $R_m$  is thus obtained as,

$$\frac{B^2(R_m)}{8\pi} = \frac{1}{2} \rho_{\text{acc}} v^2, \quad (13)$$

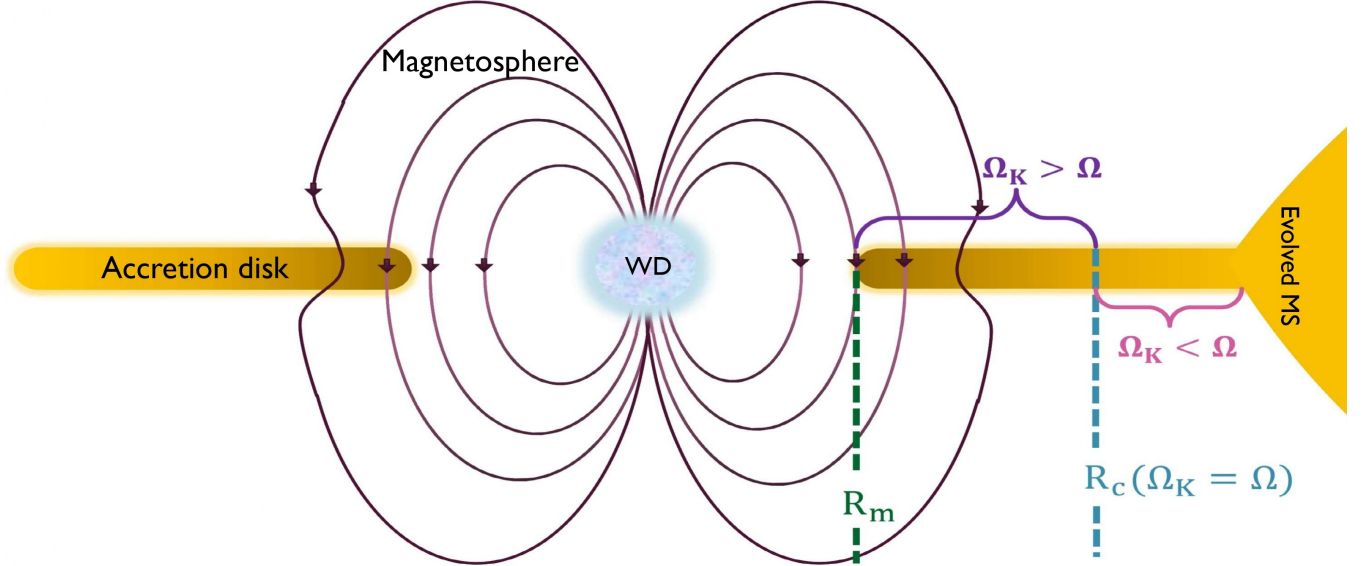


**Figure 3.** Cartoon illustration from side view of the accretion disk and magnetosphere. See text for notations.

where outside the star  $B(r) = \mu/r^3$  with dipole moment  $\mu = B_p R^3$ ,  $v = (2GM/R_m)^{1/2}$  is the free-fall speed,  $R$  is the WD radius, and  $\rho_{\text{acc}} \simeq \dot{M}_{\text{WD}}/(4\pi R_m^2 v)$ . Substituting these relations yields the standard expression for the *magnetospheric radius*

$$R_m = \xi \left( \frac{\mu^4}{2GM\dot{M}_{\text{WD}}^2} \right)^{1/7}, \quad (14)$$

with  $\xi \simeq 0.52$  for disk accretion (Ghosh & Lamb 1979b).

The Keplerian disk carries the specific angular momentum of the binary orbit whose angular velocity obeys  $\Omega_K(r) = \sqrt{(GM/r^3)}$  (Shakura & Sunyaev 1973). The inner disk generally rotates faster than the WD (Ghosh & Lamb 1979a), while the outer disk rotates more slowly (see Figure 3). The radius where the disk's Keplerian frequency equals the stellar rotation rate is the *corotation radius*,

$$R_c = \left( \frac{GM}{\Omega^2} \right)^{1/3}. \quad (15)$$

Steady accretion requires  $R_m < R_c$  so that matter can attach to stellar field lines and reach the surface. When  $R_m > R_c$  the magnetosphere rotates faster than the disk and centrifugally expels the inflow, this is the propeller regime (Ghosh & Lamb 1979b; Ghosh 1995). In our MESA implementation, this condition for accretion is enforced using `other_adjust_mdot` in `run_star_extras` as:

$$\text{mstar_dot} = \begin{cases} \dot{M}_{\text{WD}}, & R_m < R_c, \\ 0, & R_m \geq R_c, \end{cases} \quad (16)$$

so accretion is switched off whenever the WD enters the propeller regime.

## 2.5. Angular Momentum and External Torques

Having incorporated magnetic fields, rotation, and accretion into the WD structure, we now complete the model by adding the angular momentum evolution. In MESA, this is set by *angular momentum conservation* during structural readjustment as the star contracts or expands (Paxton et al. 2013). Under our assumption of solid body rotation and in the absence of external torques, the spin evolution follows as

$$\left( \frac{d\Omega}{dt} \right)_{\text{amc}} = -\frac{2\Omega}{r} \left( \frac{\partial r}{\partial t} \right)_m \left( \frac{1}{2} \frac{d \ln i}{d \ln r} \right), \quad (17)$$

where  $i$  is the specific moment of inertia of a shell at mass coordinate  $m$ . External torques enter through `extra_omega_dot` in the `other_torque` routine, ensuring they are consistently added on top of the structural term such as,

$$\left( \frac{d\Omega}{dt} \right)_{\text{total}} = \left( \frac{d\Omega}{dt} \right)_{\text{amc}} + \left( \frac{d\Omega}{dt} \right)_{\text{extra}}. \quad (18)$$

*Radiative torques.*—Magnetized, rotating WDs behave as oblique rotators when their magnetic and spin axes are misaligned, which is also consistent with the magnetic dichroism observed in several magnetic WDs (Putney 1992; Suto et al. 2023). In such systems, the extended dipolar field produces electromagnetic (EM) radiation, while the magnetic deformation along with obliquity generates a time-varying quadrupole moment and hence CGW emission. These *radiative torques* extract angular momentum from the star, driving the evolution of both  $\Omega$  and  $\chi$ , given by (Chau & Henriksen 1970; Kalita et al. 2020; Das & Mukhopadhyay 2023; Spitkovsky 2006;

Das et al. 2025)

$$\left( \frac{d\Omega}{dt} \right)_{\text{rad}} = -\frac{B_p^2 R_p^6 \Omega^3}{4c^3 I_{z'z'}} (1 + 1.1 \sin^2 \chi) - \frac{2G}{5c^5 I_{z'z'}} (I_{zz} - I_{xx})^2 \Omega^5 \sin^2 \chi (1 + 15 \sin^2 \chi), \quad (19)$$

$$I_{z'z'} \frac{d\chi}{dt} = -\frac{B_p^2 R_p^6 \Omega^2}{4c^3} \sin \chi \cos \chi - \frac{12G}{5c^5} (I_{zz} - I_{xx})^2 \Omega^4 \sin^3 \chi \cos \chi, \quad (20)$$

where  $R_p$  is the polar radius and  $I_{ij}$  are components of the moment of inertia tensor, with  $I_{z'z'} = I_{zz} \cos^2 \chi + I_{xx} \sin^2 \chi$ ;  $\hat{z}$  and  $\hat{z}'$  denote the magnetic and spin axes, respectively. The radiative contribution to  $d\Omega/dt$  is included through the `extra_omega_dot` and, as because MESA is 1D and carries no information about  $\chi$ , we evolve  $\chi$  as an auxiliary variable coupled to  $\Omega$ . Equations (19) and (20) are solved simultaneously using initial values of  $I_{xx}$ ,  $I_{zz}$ ,  $B_p$ , and  $R_p$  obtained from the two-dimensional (2D) equilibrium WD models computed with stellar structure solver XNS (see Section 3 for details) for given WD density, internal field and rotation.

*Accretion torque.*—In addition, the disk-magnetosphere coupling exerts a torque  $N_{\text{acc}}$  on the WD. If the Keplerian disk at  $R_m$  rotates faster than the magnetosphere, the WD spins up; otherwise, the magnetic linkage brakes the star. The corresponding contribution to  $d\Omega/dt$  (added through `extra_omega_dot`) is

$$\left( \frac{d\Omega}{dt} \right)_{\text{acc}} = \frac{N_{\text{acc}}}{I_{z'z'}} = \frac{n_s \dot{M}_{\text{WD}} \sqrt{GMR_m}}{I_{z'z'}}. \quad (21)$$

Here  $n_s$  is the dimensionless torque function (of  $R_m/R_c$ ) that parametrizes the disk-field coupling. In the classical GL model, the disk-field coupling is wide and extended well outside  $R_c$ , so regions with  $\Omega_K < \Omega$  contribute strongly. As a result the net torque reverses sign already at  $R_m/R_c \simeq 0.5$ , giving rise to three regimes: (i)  $R_m/R_c \lesssim 0.5$ , the WD spins up as the torque per unit area is higher near the inner disk, (ii)  $R_m/R_c \gtrsim 0.5$ , the braking region dominates, with  $n_s$  decreasing smoothly to zero and then becoming negative even while accretion continues and (iii) for  $R_m/R_c > 1$ , a dead-disk with no accretion onto the WD, and spin-down as angular momentum is transported outward through the disk. In this work we use  $n_s(R_m/R_c)$  from Ghosh & Lamb (1979b); Ghosh (1995), which spans approximately +1.3 to -0.2.

Modern MHD simulations show that field-line reconnection severely restrict the coupling region (Romanova et al. 2004); D’Angelo & Spruit (2010, 2012) – DS model captures this behavior and gives torque reversal much later, near  $R_m/R_c \approx$

**Table 1.** Observed parameters (approximately) from Odendaal et al. (2014); Tomov et al. (1998); Zang et al. (2023); Prodhan & Baruah (2018); Greiner (2000) for best studied and nearby SSS systems relevant for GW modelling.

System	$M_{\text{WD}}$ ( $M_{\odot}$ )	$M_2$ ( $M_{\odot}$ )	$\dot{M}_{\text{WD}}$ ( $M_{\odot} \text{ yr}^{-1}$ )	$\nu$ (Hz)	$d$ (kpc)
CAL 83	$\sim 1.3$	1.5–2.0	$10^{-7}$	1/67	50
RX J0019+2156	$\sim 1.3$	2.0–3.0	$10^{-7}$	—	2
RX J0925-4758	$\sim 1.3$	1.0–2.0	$10^{-7}$	—	10

0.9, with the possibility of long-lived “trapped” states where the torque switches between spin-up and spin-down. GL predicts an earlier torque reversal and hence a lower final WD spin, while DS allows prolonged spin-up before the reversal, but if the system enters a trapped state for long a time it can experience substantial long-term spin-down.

The radiative term (Equation 19) and accretion term (Equation 21) are added into the extra `extra_omega_dot` and thus Equation (18) is solved for evolution of  $\Omega$ .

## 2.6. Resulting spin evolution

We now solve Equations. (1)–(5), (7), (12), (18), (20) with MESA to follow the spin evolution of WDs in SSS. Table 1 lists the systems we target; as a fiducial case we evolve a CAL 83-like WD of initial mass  $M = 1.3 M_{\odot}$  with accretion rate of  $\dot{M}_{\text{WD}} = 10^{-7} M_{\odot} \text{ yr}^{-1}$ , and initial spin 1/67 Hz – as reported by Odendaal et al. (2014) with the X-ray pulsation study. The internal toroidal field is initialized with  $B_m \sim 10^{12} \text{ G}$ , and we assume a poloidal component with initial  $B_p \approx B_m/10^{5-6} \sim 10^6\text{--}10^7 \text{ G}$ , consistent with the moderate surface fields ( $\lesssim 10^7 \text{ G}$ ) inferred for steadily accreting WDs in SSSs (Kahabka 2006).

Three contributions shape the spin evolution: (i) the structural spin-up due to contraction during mass gain, (ii) the radiative spin-down from EM and GW torques, and (iii) the contribution from accretion torque, whose sign and magnitude depend on  $R_m/R_c$ . For the modest  $B_p$  adopted here, the EM term is negligible and the GW term becomes relevant only as  $\nu$  approaches the high end of the deciHz band; thus, throughout most of the SSS phase, the competition is primarily between contraction-driven spin-up and the accretion torque.

These behaviors are visualized in Figure 4: the top panels show the evolution of  $R_m/R_c$ , the middle panels show the individual torque contributions to  $d\Omega/dt$ , and the bottom panels show the resulting spin evolution beginning from CAL 83’s observed spin at present  $\nu = 1.5 \times 10^{-2} \text{ Hz}$ . The *first column* shows the evolution for a WD with a moderate initial surface field  $B_p \sim 10^6 \text{ G}$  using both GL and DS torques. Initially  $R_m/R_c < 0.5$ , thus the WD spins up due to accretion torque and  $R_m/R_c$  grows as spin and field increase during steady accretion. Accretion torque reversal then occurs at

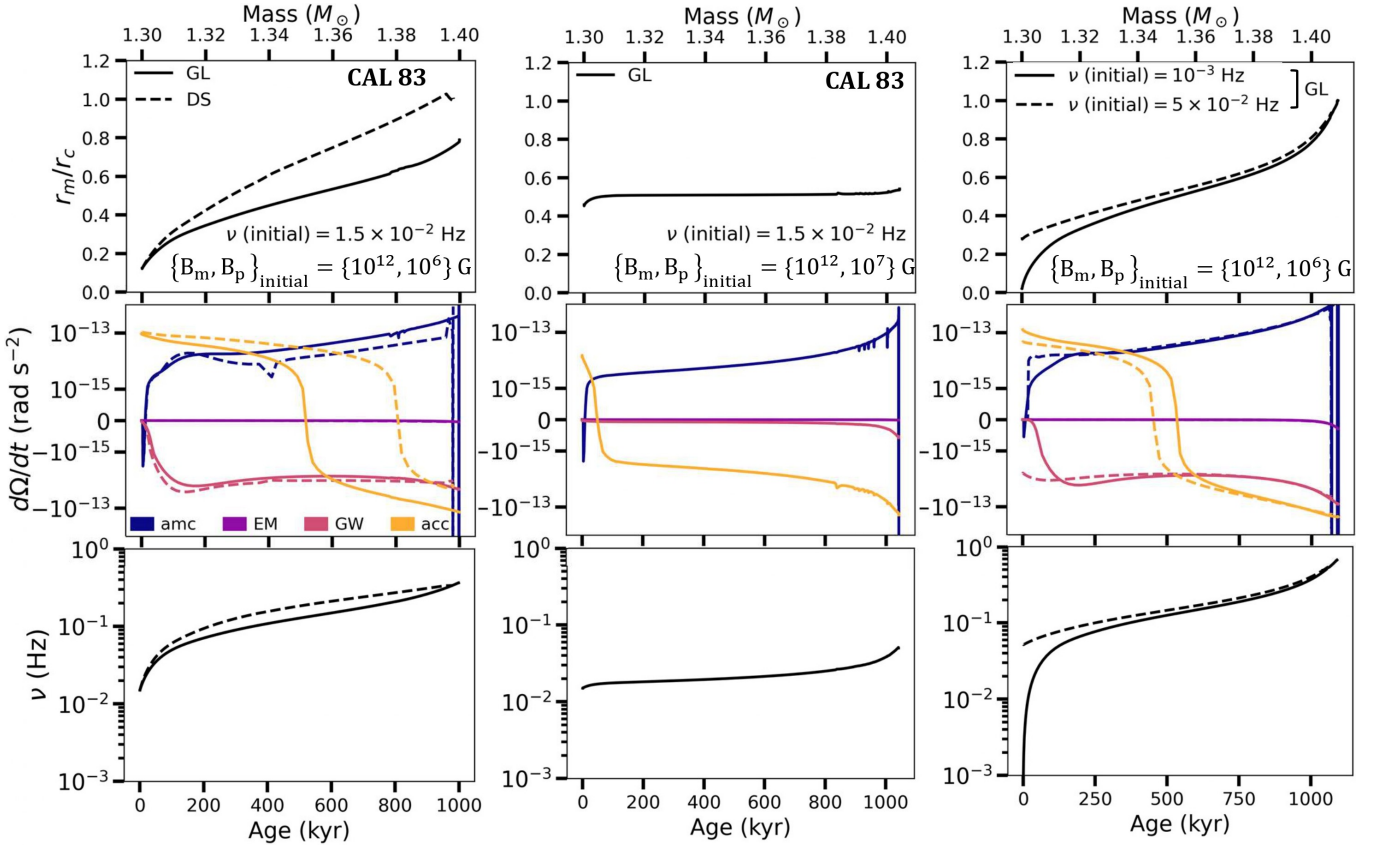


**Figure 4.** Evolution of the magnetospheric to corotation radius ratio  $R_m/R_c$  (first row), individual torque contributions to  $d\Omega/dt$  (second row), and spin frequency  $\nu$  (third row) for SSS models. The first column shows CAL 83 with  $B_p = 10^6$  G using GL (solid) and DS (dashed) torques. The second column shows a higher-field CAL 83 sequence with  $B_p = 10^7$  G using GL. The third column shows parameter studies for RX J0019+2156 and RX J0925-4758 with low ( $10^{-3}$  Hz; solid line) and high ( $5 \times 10^{-2}$  Hz; dashed line) initial spins using GL. In the second row, blue, purple, pink, and orange curves denote the structural, electromagnetic, gravitational wave, and accretion torques, respectively.

$R_m/R_c \simeq 0.5$  for GL and 0.9 for DS, leading in the GL case to an earlier shift from spin-up to either spin-down due to accretion torque only. However, depending on the balance between structural and accretion terms there is a transition from faster spin up to slower spin up. Once  $R_m/R_c > 1$ , accretion is inhibited and the WD spins down due to angular momentum transport from the star to the dead disk, and also GW, EM torques. This spin-down reduces  $R_m/R_c$ , allowing accretion to resume, which in turn drives renewed spin-up. The system, therefore, undergoes cyclic transitions between accreting and non-accreting phases as it approaches the Chandrasekhar mass.<sup>2</sup>

The DS torque produces a stronger initial spin-up due to its larger positive accretion torque, but this is progressively

offset by enhanced centrifugal support, which reduces the rate of stellar contraction and weakens the contraction-driven structural spin-up (see Appendix, Figure 9). When the accretion torque becomes negative, the structural term dominates, causing the overall spin-up in the DS case to flatten in the later phase. In contrast, the GL model shows slower spin-up at early times but maintains a relatively stronger increase at later stages when the contraction-driven structural spin-up is stronger than the DS model. As a result, DS exhibits faster early spin-up followed by a plateau, while GL shows delayed but sustained spin-up, with both models converging to a similar final spin. Thus, while the evolutionary paths differ, the terminal spin is largely insensitive to the torque prescription.

The DS model was originally developed to describe weak, channeled, or partially inhibited accretion. However, CAL 83 and SSSs in general are characterized by sustained, steady accretion. Thus, we adopt the GL torque as our default for the remaining of this work. However, we cannot meaningfully assess this choice observationally, as there is no measurement or useful limit on the spin frequency or its derivative.

<sup>2</sup> About 15-30% of  $M_2$  is expected to be supplied during the thermal mass transfer, providing  $\sim 0.5M_\odot$  of transferred material. With further wind-regulated accretion, an initially massive CAL 83 like WD can still gain enough mass ( $\sim 0.15M_\odot$ ) to reach Chandrasekhar mass within the thermal transfer phase potentially leading to a Type Ia supernova (Hachisu et al. 1999).

Since the surface magnetic field of CAL 83 is not observationally constrained, in the *second column* we explore a higher-field sequence with initial  $B_p \sim 10^7$  G. The larger magnetosphere places  $R_m/R_c$  close to the torque flip threshold ( $\simeq 0.5$ ) from the outset, limiting the efficiency of spin-up and resulting in only a slight increase in the final spin relative to the initial value. For  $B_p \gtrsim 10^7$  G,  $R_m/R_c$  would remain  $> 1$  from the beginning, suppressing accretion entirely, which is incompatible with the observed steady accretion in SSSs. We, therefore, take  $B_p \lesssim 10^7$  G as a conservative upper limit. Accordingly, we adopt  $B_p \approx 10^6$  G for the remainder of this work, as such moderate fields are better representative of the SSS population than the rare high field cases.

In the *third column*, we examine RX J0019+2156 and RX J0925–4758, which, as Galactic SSSs, would produce higher CGW strains due to their closer distances, if their frequencies are similar to CAL 83. However, there is a lack of knowledge for their measured spin frequencies. We, therefore, perform a parameter study with low ( $10^{-3}$  Hz) and high ( $5 \times 10^{-2}$  Hz) initial spins. The final spins converge to similar values despite the different starting points: models with higher initial  $\nu$  enter the accretion spin-down regime earlier owing to their larger initial  $R_m/R_c$ , while low-spin models experience a prolonged spin-up phase. Remarkably, the final spins in all cases are close to CAL 83’s present observed value, implying that comparable SSSs naturally converge to similar frequencies due to sufficient angular momentum transport from the disk, once steady accretion is established.

### 3. GRAVITATIONAL WAVE EMISSION

Having obtained the time-dependent WD structure, magnetic field and spin evolution from the MESA framework described in Section 2, we now compute the resulting quadrupolar deformation essential for GW emission. Because magnetic stresses break spherical symmetry, deformation or ellipticity cannot be extracted from the 1D MESA model. They require a full 2D magneto-hydrostatic stellar structure solver, e.g. XNS 4.0 (Pili et al. 2014; Soldateschi et al. 2021), to calculate the principal moments of inertia along different axes. For each snapshot along the MESA evolutionary track, the instantaneous  $[M, R, B_m, \Omega]$  are used as the reference to XNS to compute a corresponding 2D equilibrium model, from which we extract  $I_{xx}$ ,  $I_{zz}$  and, hence,  $\epsilon = |I_{zz} - I_{xx}|/I_{xx}$  for axisymmetric models.

#### 3.1. Magnetized equilibrium from XNS

XNS solves the coupled Einstein-Maxwell equations for stationary, axisymmetric, rotating, magnetized stars in ideal MHD. The stress-energy tensor is

$$T^{\mu\nu} = (e + P + b^2) u^\mu u^\nu - b^\mu b^\nu + \left( P + \frac{1}{2} b^2 \right) g^{\mu\nu}, \quad (22)$$

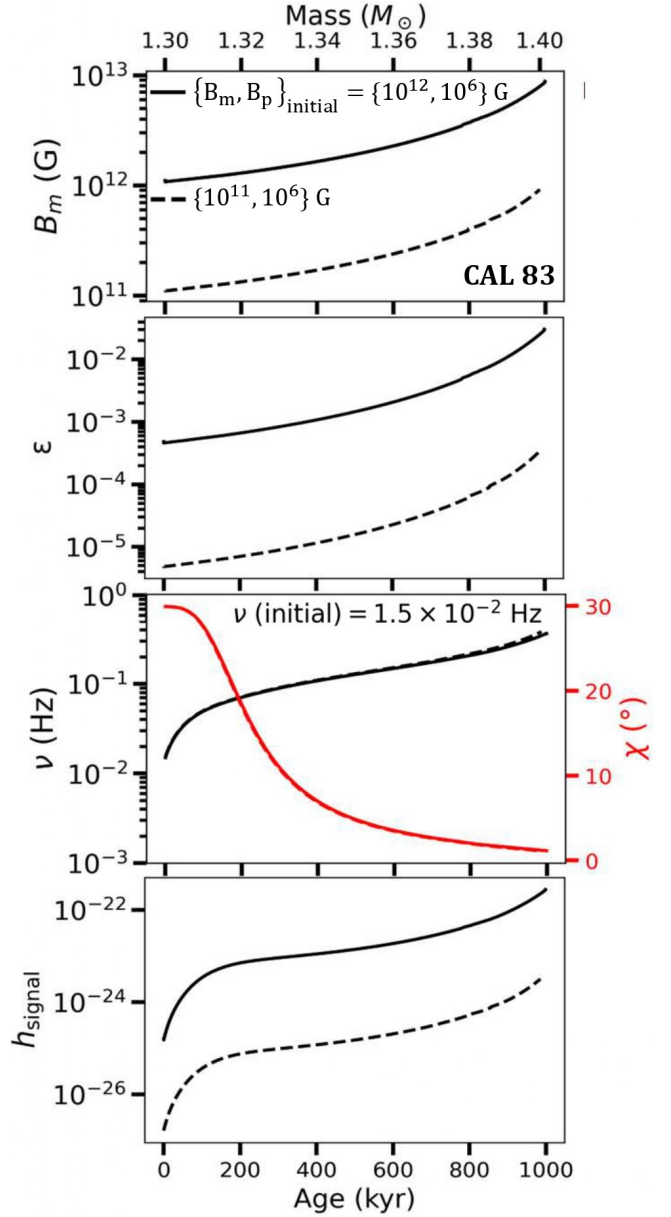


**Figure 5.** Evolution of the internal magnetic field  $B_m$  (first panel), ellipticity  $\epsilon$  (second panel), spin frequency  $\nu$  (black) and obliquity angle  $\chi$  (red; third panel), and characteristic GW strain  $h_{\text{signal}}$  (fourth panel) for CAL 83. Solid curves correspond to the fiducial model with initial magnetic field profile having maximum internal magnitude  $B_m = 10^{12}$  G while dashed curves show a comparison model with initial  $B_m = 10^{11}$  G.

where  $e$  is the energy density,  $P$  is the fluid pressure,  $u^\mu$  is the four-velocity (whose azimuthal component encodes rotation),  $b^\mu \equiv {}^*F^{\mu\nu}u_\nu$  is the magnetic field measured in the comoving (fluid) frame,  $F^{\mu\nu}$  is the electromagnetic field tensor and  ${}^*F^{\mu\nu}$  is its dual,  $B^\mu$  is the stellar magnetic field whose spatial components are  $B^r$ ,  $B^\theta$ , and  $B^\phi$ , and  $g^{\mu\nu}$  is the spacetime metric. The stellar matter satisfies magneto-

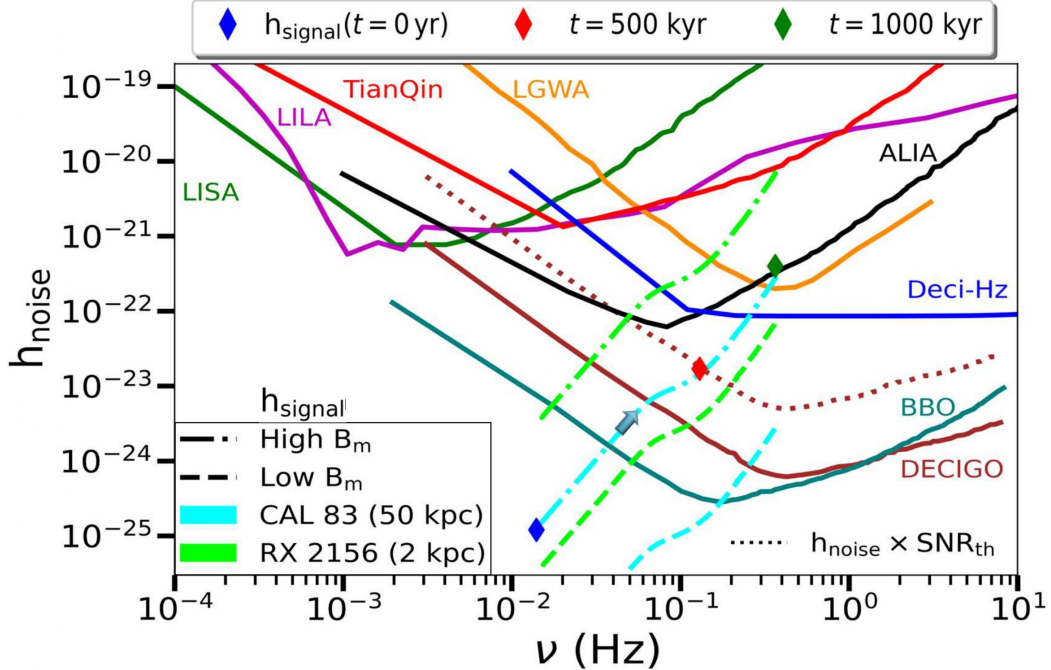


**Figure 6.** Characteristic GW strain  $h_{\text{signal}}$  for CAL 83 and RX J0019+2156 (or RX 2156), compared with the noise of milli-deciHz GW detectors. Dash-dotted and dashed curves correspond to models with initial internal magnetic fields  $B_m = 10^{12}$  G (high) and  $10^{11}$  G (low), respectively. Diamond markers indicate  $h_{\text{signal}}$  for CAL 83 (with high  $B_m$  model) at  $t = 0$  (blue), 500 kyr (red), and 1000 kyr (green) along the evolutionary track. Sky-blue curves show CAL 83 residing at  $d = 50$  kpc, while green curves show a scaled version at 2 kpc representative of RX J0019+2156. Dotted curves indicate  $\text{SNR}_{\text{th}} \times h_{\text{noise}}$  for DECIGO.

hydrostatic equilibrium condition

$$\nabla_\nu T^{\mu\nu} = 0, \quad (23)$$

together with Maxwell's equations,

$$\nabla_\nu F^{\mu\nu} = 4\pi J^\mu, \quad \nabla_\nu^* F^{\mu\nu} = 0, \quad (24)$$

where  $J^\mu$  is the four-current. Closure is provided by a cold WD equation of state, which we approximate with a relativistic polytrope  $P = K\rho^{4/3}$ , where  $K = 4.8 \times 10^{14}$  in CGS units for degenerate electron gas. This polytropic EOS differs from the temperature dependent Skye EOS used in MESA, but XNS neglects thermal effects by construction the temperature effect is negligible for the WDs (i.e.  $\rho_c$ ) under consideration.

For each chosen combination of  $\rho_c$ , internal magnetic field configuration (we use purely toroidal fields),  $B_m$ ,  $\Omega$  (assumed uniform throughout the star), XNS returns the full 2D equilibrium, including  $M$ , circumferential radius  $R$ ,  $I_{xx}$ ,  $I_{zz}$  and magnetic field profile  $B(r, \theta)$ . In this work, we compute a grid of WD equilibria with XNS spanning the relevant range of  $(\rho_c, B_{\text{max}}, \Omega)$  as found out from the WD's evolutionary track with MESA. At each time step we thus obtain  $\epsilon$  consistent with the instantaneous mass, radius, internal field, and rotation rate results from Section 2.

### 3.2. GW strain from a deformed, oblique WD

If the symmetry axis of the magnetic deformation is misaligned with the spin axis, the star emits CGWs with intrinsic GW amplitude (Bonazzola & Gourgoulhon 1996)

$$h_0 = \frac{2G}{c^4} \frac{4\pi^2 \nu^2 \epsilon I_{xx}}{d}, \quad (25)$$

where  $d$  is the source distance. The observed GW strain depends on  $\chi$  and the inclination  $i$  of the spin axis to the line of sight as:

$$h = f(\chi, i) h_0, \quad (26)$$

where  $f(\chi, i)$  encodes the relative power in the GW components at  $\nu$  and  $2\nu$ . Following DMB2025,

$$f(\chi, i) = \frac{\sin \chi}{2\sqrt{2}} \left[ (1 + \cos^2 i)^2 \sin^2 \chi + 4 \cos^2 i \cos^2 \chi \right]^{1/2} \times (2 \cos^2 \chi - \sin^2 \chi). \quad (27)$$

As XNS computes stationary, axisymmetric equilibria, after extracting  $\epsilon$  we assume a value of  $\chi$  during post-processing to calculate the GW strain. When  $\chi$  and  $i$  are unknown, we adopt the orientation-averaged value  $\langle f \rangle_{i, \chi} \simeq 0.147$  (Das et al. 2025).

Coherent integration over observation time  $T_{\text{obs}} = 4$  yr stacks  $\nu T_{\text{obs}}$  number of cycles and enhances the effective signal amplitude of source to the characteristic signal

$$h_{\text{signal}} = h_0 \sqrt{\nu T_{\text{obs}}}, \quad (28)$$

which must exceed the detector noise amplitude  $h_{\text{noise}}(\nu)$  to be detected by the detector. Thus, a signal is detectable only if the signal-to-noise ratio (SNR)

$$\text{SNR} = \frac{h_{\text{signal}}}{h_{\text{noise}}}, \quad (29)$$

exceeds the threshold  $\text{SNR}_{\text{th}} \approx 8$  for more than  $\sim 95\%$  detection efficiency (Tang et al. 2024).

To illustrate how the CGW signal from CAL 83 builds up during accretion, in Figure 5 we track the coupled evolution of  $B_m$ ,  $\epsilon$ ,  $\nu$ ,  $\chi$ , and the resulting strain  $h_{\text{signal}}$ . The solid curves correspond to our fiducial CAL 83 model with initial  $B_m = 10^{12}$  G (identical to the GL case shown in the first column of Figure 4), while dashed curves show a comparison sequence with a weaker initial field  $B_m = 10^{11}$  G.

The first panel shows the amplification of  $B_m$  driven by stellar contraction during mass growth. The second panel shows the corresponding increase in  $\epsilon$ , reflecting the increasing magnetic deformation. The third panel shows the evolution of  $\nu$  (black) together with  $\chi$  (red), evolved self-consistently using Equations (20) and (18) with an adopted initial  $\chi = 30^\circ$ . As accretion proceeds,  $\nu$  increases while  $\chi$  gradually aligns due to combined EM and GW torques. The fourth panel shows the resulting  $h_{\text{signal}}$ .

In Figure 6 we evaluate the detectability of SSSs by comparing  $h_{\text{signal}}$  computed for a coherent observation time  $T_{\text{obs}} = 4$  yr, with the noise curves of various milli-deciHz GW detectors. It shows  $h_{\text{signal}}$  for the fiducial  $B_m = 10^{12}$  G model at three representative epochs ( $t = 0, 500$ , and 1000 kyr), together with the detector sensitivities. For CAL 83, at a distance of 50 kpc (sky-blue dash-dotted curve), the signal remains below the LISA sensitivity but exceeds the detection thresholds of other next generation detectors such as Deci-Hz, DECIGO, BBO, ALIA, and LGWA for a 4 yr coherent observation once  $h_{\text{signal}} > \text{SNR}_{\text{th}} \times h_{\text{noise}}$ . For DECIGO, we explicitly show the  $\text{SNR}_{\text{th}} \times h_{\text{noise}}$  curve to illustrate the detectability.

The same figure also shows a scaled version of the CAL 83 track at a distance of 2 kpc (green dash-dotted curve), representative of the nearby Galactic SSS RX J0019+2156. Although the spin of RX J0019+2156 is unknown, our spin-evolutions (see Figure 4) demonstrate that SSSs converge to CAL 83 like frequencies once steady accretion is established, largely independent of their initial rotation. This scaling, therefore, provides a realistic estimate of its CGW detectability.

For completeness, we also include the corresponding tracks for the weaker-field case  $B_m = 10^{11}$  G (dashed curves) for CAL 83 and RX J0019+2156. Although these models produce systematically lower strains, they still approach or exceed the sensitivities of DECIGO and BBO. Since RX J0925–4758 lies at an intermediate distance ( $\sim 10$  kpc), its expected detectability follows straightforwardly from these bounds. This demonstrates that CGW detectability from SSSs is robust

across a wide and observationally unconstrained range of internal magnetic field strengths. Steady accretion simultaneously increases  $B_m$ ,  $\epsilon$ , and  $\nu$ , causing  $h_{\text{signal}}$  to grow with time and making SSSs compelling CGW sources. For known SSSs, such as CAL 83 and RX J0019+2156, where the sky position and distance are constrained, a CGW detection could probe the WD's internal magnetic field and rotation.

### 3.3. Signal to noise ratio

We now calculate cumulative SNR to assess detectability over  $T_{\text{obs}}$  with  $\mathcal{N}$  number of shorter time stacks  $T_s = T_{\text{obs}}/\mathcal{N}$  for two frequencies of GW emission is (Jaranowski et al. 1998; Maggiore 2007)

$$\langle \text{SNR} \rangle = \sqrt{\langle \text{SNR}_{\nu}^2 \rangle + \langle \text{SNR}_{2\nu}^2 \rangle}, \quad (30)$$

where

$$\langle \text{SNR}_{\nu}^2 \rangle = \frac{\sin^2 \zeta}{100} \sum_{s=1}^{\mathcal{N}} \frac{T_s h_0^2 \sin^2 2\chi}{S_n(\nu)}, \quad (31)$$

$$\langle \text{SNR}_{2\nu}^2 \rangle = \frac{4 \sin^2 \zeta}{25} \sum_{s=1}^{\mathcal{N}} \frac{T_s h_0^2 \sin^4 \chi}{S_n(2\nu)}. \quad (32)$$

Here,  $\zeta$  is the angle between the interferometer's arms:  $\zeta = 60^\circ$  for space-based detectors and  $90^\circ$  for ground-based ones. The PSD data  $S_n(\nu)$  are collected from publicly available sensitivity curves (e.g., Moore et al. 2015: <https://gwplotter.com/>).

In Figure 7, we show the cumulative SNR for a continuous 4 yr observation of CAL 83 near the end of its accretion phase, when the CGW signal is strongest (See fourth panel of Figure 5). For the fiducial  $B_m = 10^{12}$  G model, CAL 83 would be readily detectable by DECIGO and BBO. The lower panel shows the corresponding SNR for RX J0019+2156, scaled to its Galactic distance (2 kpc). Owing to its proximity, the source achieves significantly higher SNRs and would be detectable by DECIGO, BBO, Deci-Hz, ALIA, and LGWA mission well within the 4 yr mission lifetime. Because the signal peaks near the end of the accretion phase and close to the Chandrasekhar mass, a CGW detection could identify a candidate Type Ia progenitor as accreting WDs, prior to the appearance of the electromagnetic supernova explosion signature.

### 3.4. Detection probability: Number of WDs in SSSs

All such WDs should be detectable out to a maximum distance  $d$  where their signal matches the threshold detector sensitivity of DECIGO for 4 yr mission:

$$h_{\text{noise}}(\nu) = \frac{h_{\text{signal}}}{\text{SNR}_{\text{th}}} = f(\chi) \frac{2G}{c^4} \frac{4\pi^2 \nu^2}{d} \frac{\epsilon I_{xx}}{\text{SNR}_{\text{th}}} \frac{\sqrt{\nu T_{\text{obs}}}}{\text{SNR}_{\text{th}}}, \quad (33)$$

where  $f(\chi) = \langle f(\chi, i) \rangle_i$ , the averaged function over all possible inclinations, as  $i$  is not known observationally. Thus,  $d$

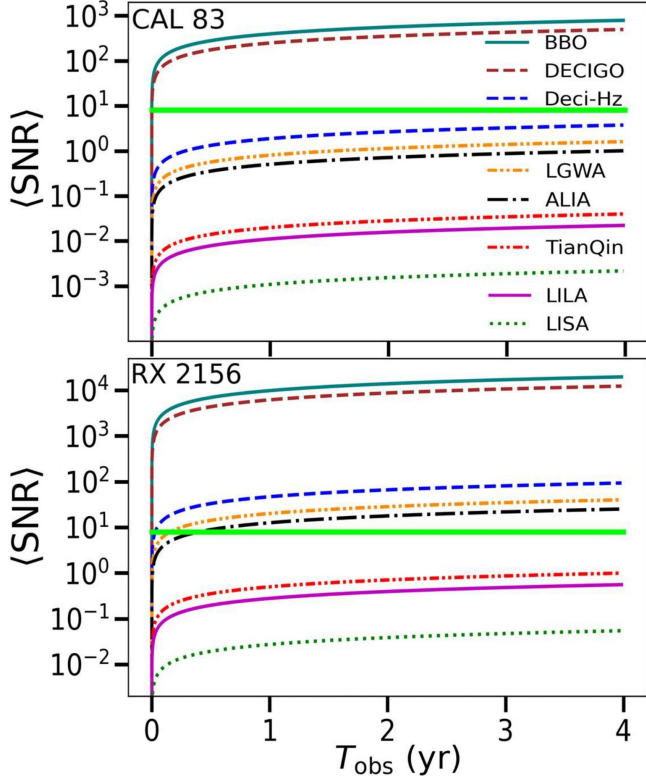


**Figure 7.** Cumulative signal-to-noise ratio (SNR) as a function of observation time  $T_{\text{obs}}$  for CGW emission from CAL 83 (top panel) and RX J0019+2156 (bottom panel), assuming the fiducial internal magnetic field  $B_m = 10^{12}$  G. The horizontal green line marks the detection threshold  $\text{SNR}_{\text{th}} = 8$ . Curves correspond to different GW detectors as labeled.

can be calculated for each  $\nu, \chi$  with  $h_{\text{noise}}$  of DECIGO and  $\epsilon$  from the simulated WD model, i.e.,

$$d(\nu, \chi) = f(\chi) \frac{2G}{c^4} \frac{4\pi^2 \nu^2 \epsilon I_{xx}}{h_{\text{noise}}(\nu)} \frac{\sqrt{\nu T_{\text{obs}}}}{\text{SNR}_{\text{th}}}. \quad (34)$$

The top panel of Figure 8 shows the maximum distance out to which DECIGO can detect SSS WDs as a function of  $\chi$  for representative spin frequencies, using the ellipticity  $\epsilon = 5 \times 10^{-4}$  of the fiducial CAL 83 model with  $B_m = 10^{12}$  G. This internal field strength need not be primordial, but can also be reached through magnetic amplification during accretion (see the first column of Figure 5). Since the obliquity is not observationally constrained for SSSs, the bottom panel shows the corresponding orientation-averaged distance  $\langle d \rangle_\chi$ . As demonstrated by the spin evolution models in Figure 4, WDs undergoing steady accretion generically reach spin frequencies  $\nu \sim 0.1$  Hz on relatively short timescales for moderate surface fields, making this frequency range representative of the SSS population.

At  $\nu \sim 0.1$  Hz, DECIGO can probe SSS WDs out to distances of  $\sim 80 - 90$  kpc for the adopted ellipticity here, encompassing the entire MW and LMC. Population synthesis

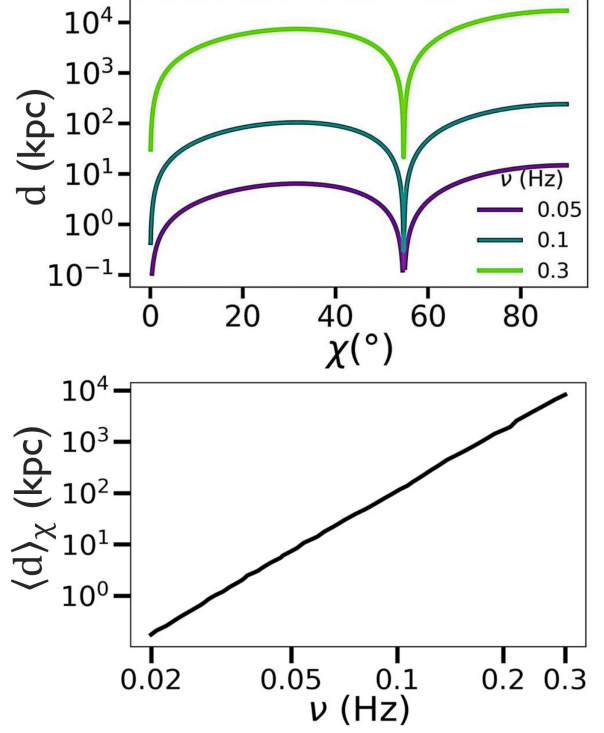


**Figure 8.** Maximum detectable distance  $d$  for CGW emission from SSS WDs with DECIGO for a 4 yr observation. Top panel:  $d$  as a function of obliquity angle  $\chi$  for representative spin frequencies  $\nu = 0.05, 0.1$ , and  $0.3$  Hz, computed using the ellipticity of the fiducial CAL 83 model with  $B_m = 10^{12}$  G. Bottom panel: orientation-averaged detection distance  $\langle d \rangle_\chi$  as a function of spin frequency  $\nu$ .

studies predict  $\gtrsim 1000$  SSSs in the Galaxy and a few hundred in the LMC (Rappaport et al. 1994), while only  $\sim 1 - 10\%$  are currently observed and others are obscured due to interstellar absorption (Greiner 2000). DECIGO's reach, therefore, implies sensitivity to the bulk of this obscured population. Even for more slowly rotating systems with  $\nu \sim 0.05$  Hz, DECIGO can probe up to distances of  $\sim 8$  kpc. Scaling by the accessible Galactic volume, this corresponds to sensitivity to  $\sim 1000 \times (8/15)^2 \simeq 280$  Galactic SSSs, demonstrating that CGW observations provide a powerful and complementary probe of the hidden SSS WD population.

### 3.5. Distinguishing GWs from Other Sources

In order to establish that a detected CGW signal originates from a WD in an SSS, it is necessary to distinguish our sources from alternative emitters in the same frequency band. In the milli Hz range, persistent GW signals are also produced by AM CVn systems (ultracompact interacting binaries) and detached double-WD binaries (DWDs), which dominate the Galactic population (Lamberts et al. 2019). These systems can appear observationally similar to CGWs from accreting WDs. The key discriminant is the ability to resolve the frequency derivative  $\dot{\nu}$  in long duration observations (Takahashi

& Seto 2002), which separates SSS accretors from the binary foreground.

AM CVn-s typically have orbital frequency derivatives of  $|\dot{\nu}| \sim 10^{-17}\text{--}10^{-16}\text{ Hz s}^{-1}$  (Gokhale et al. 2007), while DWDs can reach  $|\dot{\nu}| \sim 10^{-13}\text{ Hz s}^{-1}$  depending on their orbital frequency (Peters 1964; Maggiore 2008). Our model predicts  $|\dot{\nu}| \sim 4 \times 10^{-16}\text{--}10^{-13}\text{ Hz s}^{-1}$  (calculated from  $\nu$  evolution in Figure 5) depending on the evolutionary stage of the SSS and the initial WD spin before accretion.  $|\dot{\nu}|$  lie above DECIGO’s detectable resolution;  $\Delta\dot{\nu} \approx 3.4 \times 10^{-17}\text{ Hz s}^{-1}$  (calculated from Takahashi & Seto 2002) for a 4 yr observation with  $\text{SNR} = 8$ . The range of  $|\dot{\nu}|$  suggests clear distinction of SSS WDs from AM CVn-s, though not necessarily from DWDs. However, at frequencies  $\nu > 0.02\text{ Hz}$  the DWD population becomes essentially absent (Lamberts et al. 2019). A CGW in this frequency band is reachable for SSS WDs as soon as accretion starts (as shown in Figure 5), would therefore almost certainly originate from a WD in an SSS.

However, isolated magnetized WDs can also exhibit CGWs with  $|\dot{\nu}| \sim 10^{-15}\text{--}10^{-14}\text{ Hz s}^{-1}$  due to spin-down (i.e.,  $\dot{\nu} < 0$ ), as shown in our earlier isolated WD study, (DMB2025). In contrast, WDs in SSSs generally spin up ( $\dot{\nu} > 0$ ), which provide a robust discriminant between SSS accretors and isolated WDs as CGW sources.

#### 4. CONCLUSION

We have demonstrated that SSSs constitute a robust and physically motivated class of CGW sources, arising naturally from the coupled evolution of mass accretion, magnetic field amplification, and rotational spin-up in WDs. By consistently linking time-dependent WD evolution with MESA to magnetized equilibria obtained from the Einstein-Maxwell solver XNS, we have quantified the magnetic deformation and CGW emission throughout the SSS phase.

Our results show that steady accretion drives internal toroidal fields to  $B_m \sim 10^{12} \text{--} 10^{13}\text{ G}$  and induces ellipticities  $\epsilon \sim 10^{-6} \text{--} 10^{-2}$  in massive WDs. At the same time, disk-field coupling and contraction-driven spin-up lead toward spin frequencies  $\nu \sim 0.05 \text{--} 0.3\text{ Hz}$ , depending on the initial dipolar magnetic field, but largely independent of the initial rotation.

The resulting CGW from well-studied SSSs such as CAL 83 in LMC grows during the accretion phase and becomes detectable by planned detectors such as DECIGO, BBO for multi-yr coherent observations, while remaining below LISA sensitivity. Nearby galactic SSSs such as RX J0019+2156 emerge as higher SNR CGW sources, thus can be also detectable by Deci-Hz, ALIA, LGWA. Importantly, detectability

remains robust across two-three order of magnitude uncertainty in the internal magnetic field strength, underscoring that CGW emission is a generic outcome of accretion in SSSs rather than a fine tuned scenario.

CGW observations further provide a powerful probe of the obscured SSS population. Depending on the ellipticities and spins of WDs in SSSs, DECIGO can access the SSS population in our Galaxy and Magellanic Clouds, implying sensitivity to hundreds to thousands of systems that remain undetected in soft X-rays. The sign and magnitude of  $\dot{\nu}$  offer a clear discriminator against the dominant milli Hz foreground from detached DWDs and AM CVn-s, and also distinguish accreting SSS WDs from isolated WD CGW emitters.

Finally, a targeted CGW detection from known SSSs such as CAL 83, RX J0019+2156, RX J0925-4758 would directly probe the WD’s internal magnetic field and rotation. CGW detection from a near-Chandrasekhar SSS could also identify the system as a potential pre-explosion Type Ia progenitor candidate. Our results establish SSSs as prime CGW targets for upcoming deciHz missions and motivate dedicated targeted and blind searches as a new window onto rapidly rotating, magnetized, accreting WDs in the local Universe.

#### ACKNOWLEDGMENTS

MD thank Nils Andersson for suggestions about magnetic field, David Bour for discussion about MESA, and Soumallya Mitra for insightful discussions on computational implementation. She also acknowledges the Prime Minister’s Research Fellowship (PMRF) scheme, with Ref. No. TF/PMRF-22-5442.03. TB acknowledges support of the Polish National Science Center (NCN) grant 2023/49/B/ST9/02777 and grant Maestro (2018/30/A/ST9/00050). BM acknowledges a project funded by SERB, India, with Ref. No. CRG/2022/003460, for partial support towards this research.

#### APPENDIX

Figure 9 illustrates the evolution of the WD radius (top row) and the resulting magnetic field amplification (bottom row) due to radial contraction for the models discussed in Section 2.6. The first column shows that the DS torque leads to enhanced centrifugal support, which slows stellar contraction relative to the GL case and weakens the contraction-driven structural spin-up. This effect explains the late-time flattening of the DS spin evolution when the accretion torque becomes negative and contraction-driven structural spin-up is the only dominant part, as seen in Figure 4. The remaining columns correspond directly to the other columns shown in Figure 4.

#### REFERENCES

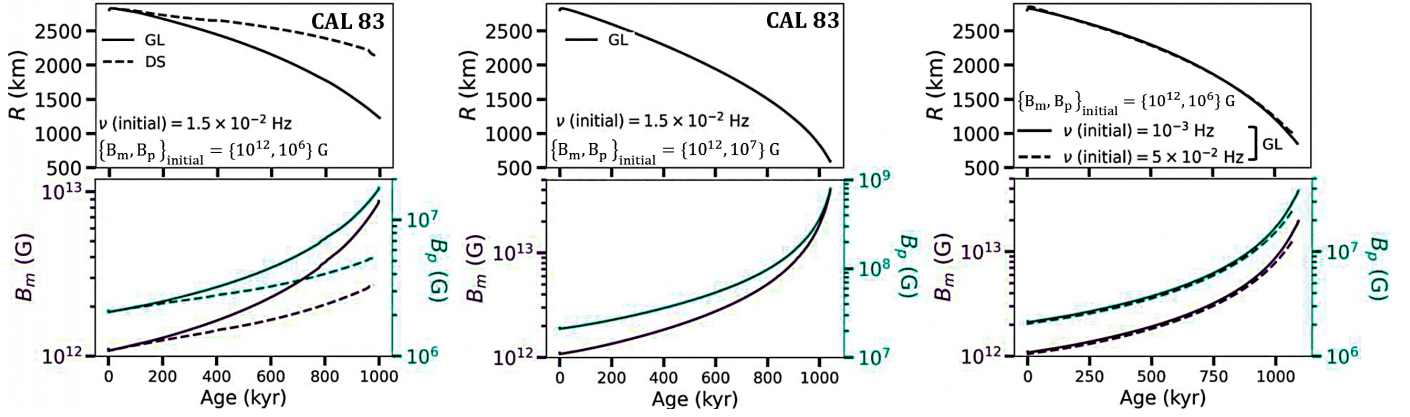


**Figure 9.** Evolution of the WD radius (top panels), and internal toroidal ( $B_m$ ) and surface poloidal ( $B_p$ ) magnetic fields (bottom panels) for accreting WD models. The columns correspond to the same models shown in Figure 4.

Bonazzola, S., & Gourgoulhon, E. 1996, A&A, 312, 675

Braithwaite, J. 2009, MNRAS, 397, 763

Braithwaite, J., & Spruit, H. C. 2006, A&A, 450, 1097

Chau, W. Y., & Henriksen, R. N. 1970, ApJ, 161, L137

Colpi, M., Armano, M., Audley, H., et al. 2024, arXiv e-prints, arXiv:2402.07571

Creighton, T., et al. 2025, arXiv e-prints, arXiv:2508.18437

Crowder, J., & Cornish, N. J. 2005, PhRvD, 72, 083005

Cumming, A. 2002, MNRAS, 333, 589

Cutler, C., & Harms, J. 2006, PhRvD, 73, 042001

D'Angelo, C. R., & Spruit, H. C. 2010, MNRAS, 406, 1208

—. 2012, MNRAS, 420, 416

Das, M., & Mukhopadhyay, B. 2023, ApJ, 955, 19

Das, M., Mukhopadhyay, B., & Bulik, T. 2025, ApJ, 995, 107

Endal, A. S., & Sofia, S. 1976, ApJ, 210, 184

Ferrario, L., de Martino, D., & Gänsicke, B. T. 2015, Space Science Reviews, 191, 111

Ghosh, P. 1995, ApJ, 453, 411

Ghosh, P., & Lamb, F. 1979a, ApJ, 232, 259

Ghosh, P., & Lamb, F. K. 1979b, ApJ, 234, 296

Gokhale, V., Peng, X. M., & Frank, J. 2007, ApJ, 655, 1010

Goldreich, P., & Reisenegger, A. 1992, ApJ, 395, 250

Greiner, J. 1991, A&A, 246, L17

—. 2000, New Astronomy, 5, 137

Hachisu, I., & Kato, M. 2003, ApJ, 598, 527

Hachisu, I., Kato, M., & Nomoto, K. 1999, ApJ, 522, 487

Heyl, J. S. 2000, MNRAS, 317, 310

Heyl, J. S., & Kulkarni, S. R. 1998, ApJ, 506, L61

Jaranowski, P., Królak, A., & Schutz, B. F. 1998, PhRvD, 58, 063001

Jermyn, A. S., Schwab, J., Bauer, E., Timmes, F. X., & Potekhin, A. Y. 2021, ApJ, 913, 72

Kahabka, P. 1995, A&A, 304, 227

Kahabka, P. 2006, Advances in Space Research, 38, 2836

Kalita, S., Mukhopadhyay, B., Mondal, T., & Bulik, T. 2020, ApJ, 896, 69

Kawamura, S., Nakamura, T., Ando, M., et al. 2021, Progress of Theoretical and Experimental Physics, 2021, 05A105

Lamberts, A., Blunt, S., Galloway, D., et al. 2019, MNRAS, 490, 5888

Maggiore, M. 2007, Gravitational Waves. Vol. 1: Theory and Experiments, Oxford Master Series in Physics (Oxford University Press)

—. 2008, Gravitational Waves: Volume 1: Theory and Experiments (Oxford University Press), doi:10.1093/acprof:oso/9780198570745.001.0001

Mei, J., Luo, J., Wang, G., & et al. 2021, Progress of Theoretical and Experimental Physics, 2021, 05A107

Moore, C. J., Cole, R. H., & Berry, C. P. L. 2015, Classical and Quantum Gravity, 32, 015014

Motch, C., Hasinger, G., & Pietsch, W. 1994, Astron. Astrophys., 284, 827

Mukhopadhyay, B., & Bhattacharya, M. 2022, Universe, 8, 626

Nomoto, K. 1979, ApJ, 234, 159

Nomoto, K., Saio, H., Kato, M., & Hachisu, I. 2007, ApJ, 663, 1269

Norton, A. J., Somerscales, R. V., & Wynn, G. A. 2004, ApJ, 614, 349

Odendaal, A., Meintjes, P. J., Charles, P. A., & Rajoelimanana, A. F. 2014, MNRAS, 437, 2948

Paxton, B., Bildsten, L., Dotter, A., et al. 2011, ApJS, 192, 3

Paxton, B., Cantiello, M., Arras, P., et al. 2013, ApJS, 208, 4

Paxton, B., Marchant, P., Schwab, J., et al. 2015, ApJS, 220, 15

Paxton, B., Smolec, R., Schwab, J., et al. 2019, ApJS, 243, 10

Peters, P. C. 1964, Physical Review, 136, B1224

Pili, A. G., Bucciantini, N., & Del Zanna, L. 2014, MNRAS, 439, 3541

Prodhani, N., & Baruah, M. 2018, Journal of Astrophysics and Astronomy, 39, 9

Putney, A. 1992, ApJ, 390, L67

Quentin, L. G., & Tout, C. A. 2018, MNRAS, 477, 2298

Rappaport, S., Di Stefano, R., & Smith, J. D. 1994, ApJ, 426, 692

Romanova, M. M., Ustyugova, G. V., Koldoba, A. V., Wick, J. V., & Lovelace, R. V. E. 2004, ApJ, 610, 920

Shakura, N. I., & Sunyaev, R. A. 1973, A&A, 24, 337

Soldateschi, J., Bucciantini, N., & Del Zanna, L. 2021, A&A, 654, A162

Spitkovsky, A. 2006, ApJL, 648, L51

Suto, Y., Ohsuga, K., & Fujimoto, M. Y. 2023, Publications of the Astronomical Society of Japan, arXiv:2301.00693

Takahashi, R., & Seto, N. 2002, ApJ, 575, 1030

Tang, P., Eldridge, J. J., Meyer, R., et al. 2024, MNRAS, 534, 1707

Tomov, T., Munari, U., & Kolev, D. 1998, Astron. Astrophys., 333, L67

Trümper, J., Hasinger, G., Aschenbach, B., Braeuninger, H., & Briel, U. 1991, Nature, 349, 579

van den Heuvel, E. P. J., Bhattacharya, D., Nomoto, K., & Rappaport, S. A. 1992, A&A, 262, 97

Wickramasinghe, D. T., Tout, C. A., & Ferrario, L. 2014, MNRAS, 437, 675

Wolf, W. M., Bildsten, L., & Brooks, J. 2013, ApJ, 777, 136

Yi, S., Lau, S. Y., Yagi, K., & Arras, P. 2024, MNRAS, 531, 4681

Zang, L., Qian, S.-B., & Fernández-Lajús, E. 2023, MNRAS, 522, 2732